Computational Screening of Oxide Perovskites as Insertion-Type Cathode Material

Johannes Döhn[†] and Axel Groß[*,†,‡]

†*Institute of Theoretical Chemistry, Ulm University, Oberberghof 7, 89081 Ulm, Germany*

‡*Helmholtz Institute Ulm (HIU) for Electrochemical Energy Storage, Helmholtzstraße 11, 89081 Ulm, Germany*

E-mail: axel.gross@uni-ulm.de

Abstract

The electrification of the transportation sector exacerbates all issues concerning the use of critical materials in state-of-the-art batteries and, therefore, urges the development of new technologies based on potentially greener and more abundant materials. One research trend is the substitution of Li as shuttle ion with other elements such as Na, K, Mg, Ca, Zn, Al i.e. the so-called post Li technology. Although signficant progress has been achieved in this field recently, these novel battery chemistry have mostly not matured yet. In the present work we contribute to the development of new battery materials by screening the materials' class of oxide perovskites as high-energy insertion-type cathode material. Based on density functional theory calculations, the specific energy, the energy density, the volume change, and the energy above hull were derived for 280 compounds and appropriate screening criteria were employed. In a second step, the diffusion barriers were determined for the most suitable materials. Eventually, we suggest $MgNbO_3$, $ZnVO_3$, and $AlMoO_3$ as candidate materials for further investigation with $MgNbO_3$ appearing particularly promising.

Introduction

The electrification of transportation devices is widely regarded as crucial for the transition towards renewable energy systems[1–3] but, while electric vehicles (EV) based on hydrogen fuel cells continuously suffer from high fuel costs due to unfavorable round trip efficiencies,[4,5] the price for Li-ion batteries, scaled by their energy capacity, has been reduced by about 97 % since market introduction in 1991, accompanied by significant performance gains.[6] Accordingly, the growth of the battery market for light duty EVs exceeds all expectations[7–9] and batteries are at least considered as viable options for heavy duty EVs[10] and short to medium distance shipping.[11] The consequence of this ongoing trend is the steeply rising demand for the materials used, escalating all the environmental, geo-political and social challenges in their acquisition.[12–14] A circulatory material flow could offer remedy in the described scenario, but issues concerning sustainable manufacturing[15] and recycling[12,16] of currently used battery materials are not fully resolved yet. Therefore, it does not come as a surprise that the employment of more abundant and potentially greener materials has been suggested by several authors.[17–19]

In order to suffice user demands on range and flexibility of mobile applications, one particular requirement on the energy storage is high energy density and/or high specific energy.[20] Concerning batteries, although substantial improvements on the engineering level have been made recently, on the materials' side there are so far no post-Li alternatives reaching up to the performance of state-of-the-art technologies based on lithium ion shuttles.[8,9] One research trend, therefore, aims at rendering Li-ion technology more sustainable. This can obviously be done by replacing critical materials with less critical ones, as is reflected in the trend towards Co- and Ni-free LFP cathodes[21] or in the substitution of natural graphite by the synthetic equivalent.[22] Also performance enhancement of current technology may decrease the materials exploitation, for example by increasing the cycle life of the battery or by elevating the energy that can be stored in a certain amount of material. A completely different but recently strongly pronounced idea is the substitution of Li as the shuttle ion.

1

Due to chemical similarity, the most obvious candidate is the earth abundant element Na. Unfortunately, although material classes from Li-ion battery technology can also be used for Na-ion batteries, they do not reach the same performance. [23-25] This problem is even more pronounced for other considered shuttle ions such as K, Mg, Ca, Zn and Al. As a result, a complete research field focusing on the development of corresponding materials has evolved during the last years. [26] Many reviews highlight the progress in the field, [27-31] but the ultimate chemistries have yet to be found and the corresponding materials have to be developed.

One in many regards particularly interesting class of materials are oxide perovskites, which are named after the Russian politician and leisure time mineralogist L. A. Perovski, who allegedly enabled the discovery of the prototype crystal $CaTiO_3$ with its typical corner-sharing oxygen octahedra. [32] The first application of this class of materials was $BaTiO_3$, which has served as dielectric medium in capacitors since the 50s of the last century. [33] Research then became aware of the tuneability of these materials' properties by substituting the cations on the A- and B-position in ABO_3, which together with the oftentimes straightforward synthesizability led to a range of applications. Examples can be found in catalysis and electrocatalysis [34] but oxide perovskites are also used as ionic conductors in solid oxide fuel cells [35] or as supercapacitors. [36]

Despite their popularity, oxide perovskites have hardly been studied for their use in post-Li systems. $Li_xLa_{1-x}TiO_3$ has been discussed as potential solid electrolyte material for Li-ion batteries but intercalation of Na and Mg was not feasible. [37,38] On the cathode side, $CaMO_3$ (M=Cr, Co, Fe, Mn, Ni, Mo) has been studied with first-principles methods but no electrochemical activity could be observed for the suggested material $CaMoO_3$ in a subsequent experiment. [39] On the other hand, Ca intercalation into $CaMnO_3$ has been reported, although the process was accompanied by partial degradation of the material. [40] To the best of our knowledge a more comprehensive investigation of oxide perovskites with respect to battery materials particularly for post-Li technology is still lacking.

2

In order to fill this gap we employed density functional theory (DFT) which is well-suited to describe battery components on the atomic level [41] to systematically investigate the materials' class of oxide perovskites as potential high-energy cathode materials for the intercalation of the above mentioned shuttle ions. In total, we performed DFT calculations on 280 different compounds and we evaluated different properties such as theoretical specific energy, theoretical energy density, theoretical volume change, and chemical stability. For those candidate materials with promising properties we additionally evaluated the diffusion barrier of the corresponding ion. Eventually, we were able to narrow down the initial material space to the three compounds $MgNbO_3$, $ZnVO_3$, and $AlMoO_3$ which we suggest for further investigation. $MgNbO_3$ seems to be the most promising candidate material among these three.

Calculational Details

Oxide perovskites have the general stoichiometry ABO_3 where the B-site cation is octahedrally coordinated with oxygen and the A-site cation resides in the interstitial voids of these corner-sharing octahedra. The ideal cubic structure only contains five atoms per unit cell, but many real compounds are subject to distortions of this highly symmetric phase leading to a wide range of geometries with lower symmetry still fulfilling the above given structural definition. These distortions can be classified in three categories: i) Tilting of the octahedra as famously described by A.M. Glazer. [42,43] ii) Jahn-Teller distortions of the octahedra. iii) Ferroelectrical displacement of the B-site cations within the octahedra. [44] It has been shown in a DFT analysis that the energy is lowered significantly (several 100 meV/atom) by structural distortions so the highly symmetric cubic phase is not realized in many compounds. [45] On the other hand, combining only the distortions of type i) and iii) gives rise to 61 symmetrically non-equivalent geometries, [44] a number which is far too large for the screening of several hundred compounds. Therefore, we decided to follow the rather pragmatic approach
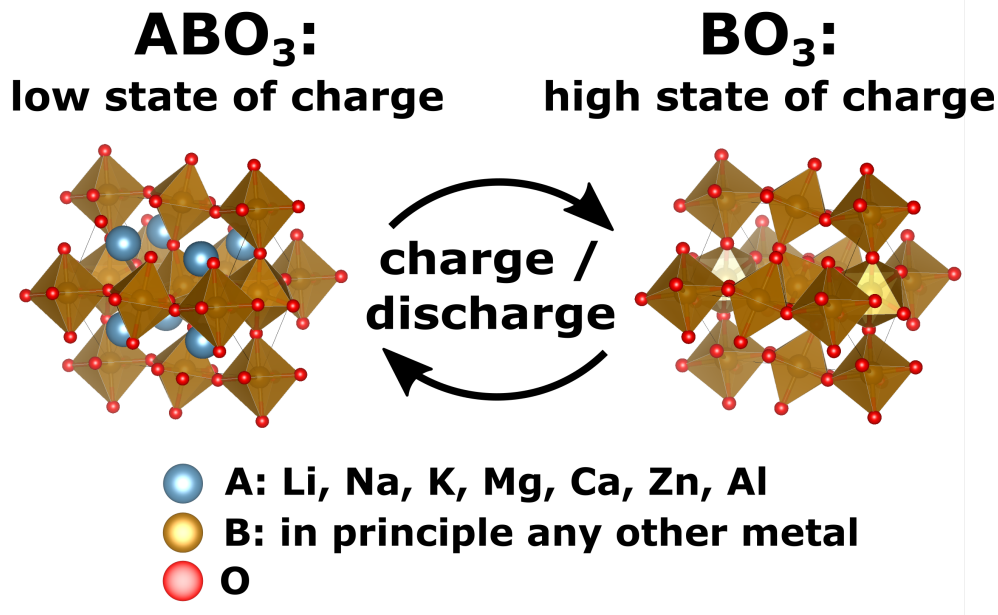
3

ABO₃:
low state of charge

BO₃:
high state of charge

charge / discharge

🔵 **A: Li, Na, K, Mg, Ca, Zn, Al**
🟡 **B: in principle any other metal**
🔴 **O**

Figure 1: Battery cathode materials based on the perovskite stucture considered in this study. The fully intercalated material ABO_3 represents the low state of charge while the fully deintercalated material BO_3 represents the high state of charge of the cathode material in the battery. All structures were restricted to perovskite geometry.

of Emery and Wolverton [46] and only evaluate the most common perovskite geometries i.e. the cubic phase (Pm$\bar{3}$m), the rhombohedral phase (R$\bar{3}$c), the tetrahedral phase (P4mm) and the orthorhombic phase (Pnma) for every input stoichiometry.

To study insertion-type cathode materials, the A-site has to be occupied by one of the typically considered shuttle ions Li, Na, K, Mg, Ca, Zn, Al while the BO_6 octahedra serve as host structure for the topotactic intercalation reaction. The B-side can at least in principle be occupied by any other metal of the periodic table,[47] but for our screening we chose a rather practical approach and excluded all elements (i) which are not stable (Tc, Pm, the elements beyond Bi), (ii) which are too toxic for any real live technology (Be, As, Cd, Te, Hg, Tl, Pb), (iii) which are too rare for any large scale application (Ru, Rh, Pd, Re, Os, Ir, Pt, Au) and (iv), although we allowed for stoichiometries with untypical oxidation states, we excluded alkali and alkaline earth metals due to their inertness to take up and release electrons. This gives us in in total $7 \cdot 40 = 280$ different stoichiometries ABO_3 as input for the investigations.

4

Furthermore, we focus on high-energy materials which enable the complete deinsertion of the A-site cations. Therefore, we modelled the cathode material in the low state of charge i.e. ABO_3 and in the high state of charge i.e. BO_3 as depicted in Figure 1. Each structure was modelled in the four above mentioned geometries and the lowest energy structure was used for the investigation of the battery properties. Topotacticity of the intercalation reaction is thus introduced by restricting both the low state of charge and the high state of charge to a perovskite geometry although exactly the same symmetry is not necessarily demanded.

The ground state energy of every input structure was calculated using DFT employing the exchange-correlation functional suggested by Perdew, Burke, and Ernzerhof.[48] Oxide materials are known to exhibit self-interaction errors,[49–51] hence we added an on-site interaction term U in the functional form suggested by Dudarev et al.[52] with values of U_{Co}=3.32, U_{Cr}=3.7, U_{Fe}=5.3, U_{Mn}=3.9, U_{Mo}=4.38, U_{Ni}=6.2, U_{V}=3.25, and U_{W}=6.2. Note that this is on par with the functional as applied by the Materials Project database,[53] rendering the calculations comparable. The ionic cores were treated with the Projector Augmented Wave method[54] as implemented in the Vienna Ab Initio Simulation Package.[55–57] Electronic wave functions were expanded up to energies of 600 eV and it was made sure that total energies converged within a few meV/atom with respect to the number of k-points in the first Brillouin zone. All structures were optimized until the entries of the stress tensor and all forces were below 0.01 eV/Å without constraining any internal degree of freedom. The spin-state of many perovskites is still subject to ongoing debate[58] and the difference in ferromagnetic and non-magnetic states may easily result in energetic errors of more than 1 eV/atom. Furthermore, it is well known[59] and also confirmed by our experience that sometimes the correct non-magnetic ground state is not found when the calculation is initialized ferromagnetically. Therefore, we explicitly searched for high-spin and low-spin states for all possibly magnetic elements,[59] while all other elements were initialized with low magnetic moment. No attempt was made to find antiferromagnetic states as this approximation typically results only in low

5

energetic errors compared to ferromagnetic states[60] and the exact magnetic ordering is of no particular interest for the present study.

Theoretical specific energy ρ_{grav} and theoretical energy density ρ_{vol}, both evaluated with respect to metal anode, have been approximated by

$$\rho_{grav} \;=\; \frac{E_{\mathrm{ABO_3}} - E_{\mathrm{BO_3}} - E_{\mathrm{A}}}{M_{\mathrm{ABO_3}}} \quad \text{and} \quad \rho_{vol} \;=\; \frac{E_{\mathrm{ABO_3}} - E_{\mathrm{BO_3}} - E_{\mathrm{A}}}{V_{\mathrm{ABO_3}}} \;, \tag{1}$$

where $E_{\mathrm{ABO_3}}$ and $E_{\mathrm{BO_3}}$ are the DFT energies of the cathode materials in the corresponding state of charge and E_{A} is the DFT energy of the metallic species A. $M_{\mathrm{ABO_3}}$ and $V_{\mathrm{ABO_3}}$ are the mass and the volume of the perovskite materials per formula unit. Zero-point energies and entropic contributions were neglected for all energetic considerations. The theoretical volume change was obtained by

$$\frac{\Delta V}{V} \;=\; \frac{V_{\mathrm{ABO_3}} - V_{\mathrm{BO_3}}}{V_{\mathrm{ABO_3}}} \;. \tag{2}$$

Chemical stability and synthesizability were addressed by comparing a compound's energy with all possible configurations with the same stichioemtry that are available in the Materials Project database.[59] The difference to the configuration with the lowest energy, commonly termed the energy above hull E_{hull}, was then evaluated. A few remarks on the calculation procedure are noteworthy: As described above, we used the same functional form as the Materials Project database, rendering the calculations in principle comparable. Nevertheless, deviating input parameters with respect to the basis set and the particular choice of the pseudopotentials can lead to differences in the resulting total energies. In order to minimize these deviations, not total energies but formation energies were compared. Two other problems arise due to this necessary procedure: i) It is well-recognized that the O_2 molecule is overbound in GGA calculations leading to erroneous results for the formation energies of oxide species. ii) Some compounds were calculated with the PBE+U functional, whereas, for the metallic elemental phases, the original functional was used, again resulting in poor

6

estimations for the formation energies. In order to account for these errors, we adapted the empirical corrections described by Wang et al.[61] Note also that we allowed negative values of E_{hull} which means that the considered compound is lower in energy than the convex hull spanned by the compounds of the database.

Nudged elastic band (NEB) calculations [62] were employed to evaluate the diffusion barrier E_{diff} of certain species. The $A_x BO_3$ supercells were created with $x = 0.0555/0.0625$ in the high vacancy limit and $x = 0.9445/0.9375$ in the low vacancy limit, where the first number corresponds to cubic and tetragonal cells and the second one to rhombohedral and orthorhombic ones. We investigated all symmetrically non-equivalent diffusion paths i.e. one for cubic and rhombohedral cells, two for tetragonal and three for orthorhombic ones. The calculations were performed with five images, only in some cases with convergence issues the number was reduced to four or three. Optimized NEB algorithms[63] were used to optimize the ion positions until the forces on every ion were lower than 0.05 eV/Å. The climbing image method was used to ensure that the transition state was found.[64]

Results

We will now describe our approach to screen the oxide perovskite materials. As described above, the full or empty electrode materials ABO_3 and BO_3, respectively, were considered in four different symmetries each. The one lowest in energy was then used for all further investigations. It has already been mentioned that in a previous study distorted perovskites

Table 1: Battery properties of state-of-the-art cathode materials. The battery properties for LCO, LMO, and LFP were derived based on the DFT calculations of Chevrier et al.[65] as described in the Calculational Details. The threshold criteria have been derived in order to screen the materials properties of Figure 3.

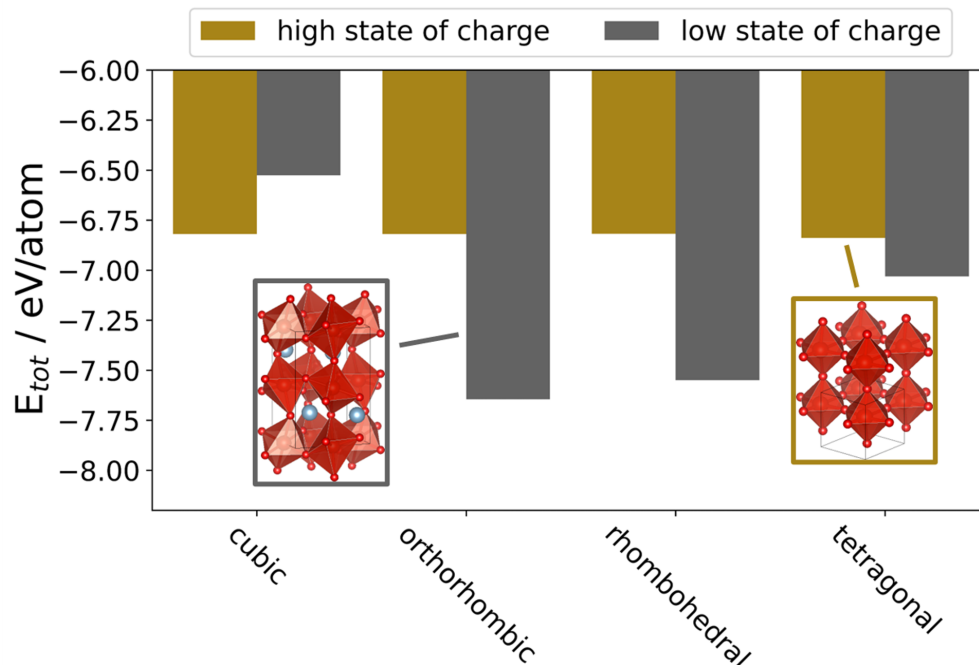| Property	LCO	LMO	LFP	Screening Criterion
ρ_{grav} [Wh/kg]	1054	599	589	> 500
ρ_{vol} [Wh/dm^3]	5214	2434	2056	> 2000
$\frac{\Delta V}{V}$ [%$_{abs}$]	3.47	4.25	4.45	< 10

Figure 2: Total energy per atom for the different distortions of VO_3 and $AlVO_3$ as example. The lowest energy structures are depicted for both cases. The structure of VO_3 is almost cubic and the different modelled distortions hardly differ in energy, whereas in $AlVO_3$ the octahedra are severely tilted and distorted and the orthorhombic phase is more than 1 eV/atom lower in energy than the ideal cubic phase.

deviated by several 100 meV/atom from the cubic structure.[45] Our investigation reveals that the difference may even be in the order of one eV/atom as is deduced from the comparison of the total energies of the different polymorphs of VO_3 and $AlVO_3$ in Figure 2. While for some of the analysed compounds as for instance VO_3 the energy difference between the polymorphs is only a few meV/atom and the lowest-energy geometry only slightly deviates from the cubic structure, the octahedra in other compounds as for instance $AlVO_3$ are considerably tilted and distorted leading to significant deviations in energy. This confirms once more that the cubic structure is an invalid approximation in many cases and taking into account the less symmetric phases is clearly necessary. In general, of all 280 ABO_3/BO_3 stoichiometries 206/161 attained the lowest energy in the orthorhombic phase, 52/77 in the rhombohedral phase, 17/42 in the tetrahedral phase and 5/0 in the highly symmetric cubic phase.

The battery properties which are are directly accessible from the calculations are depicted
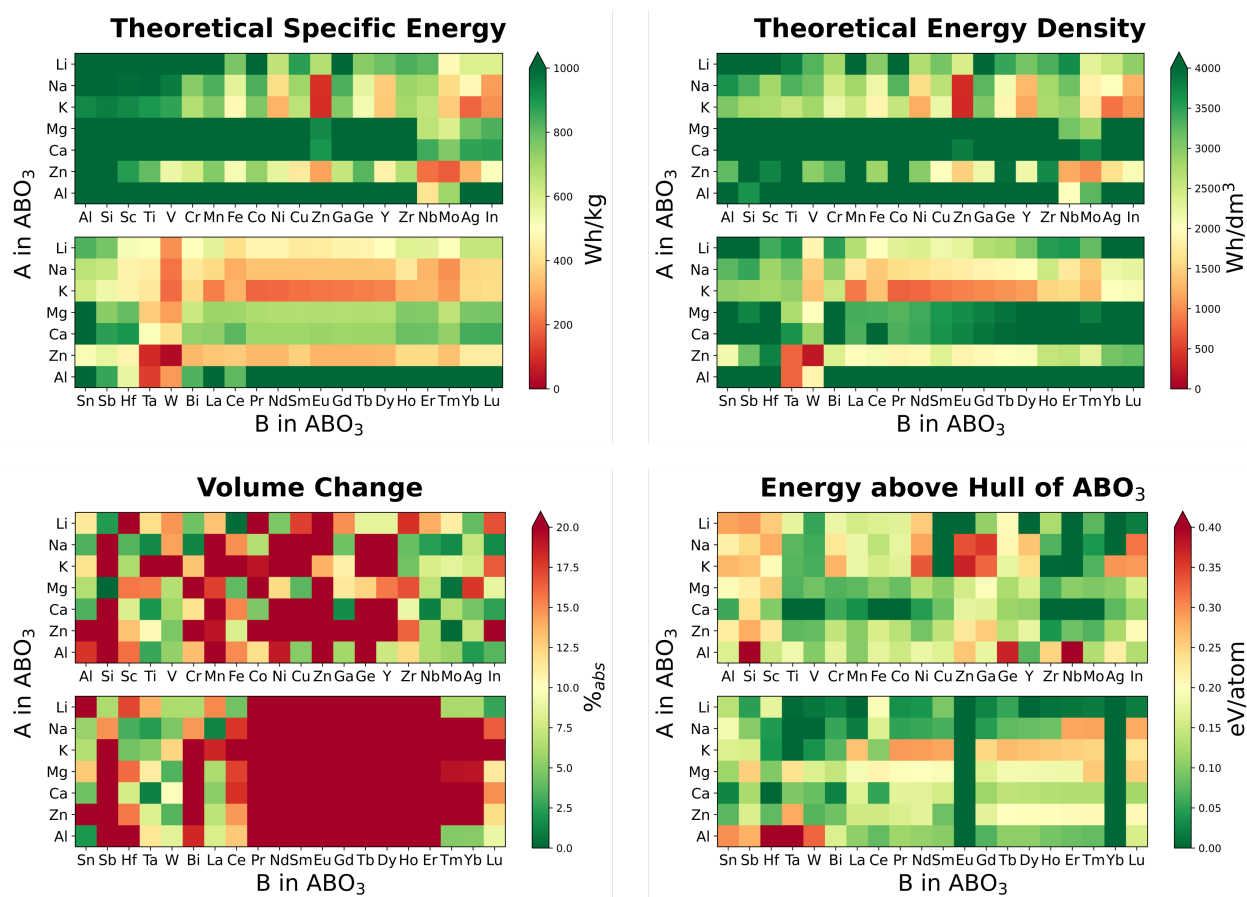
8

Figure 3: Derived battery Properties for 280 ABO_3 compounds. Green indicates preferable values for the given property whereas red means the opposite. This is why the color code goes from red (low values) to green (high values) in the case of the theoretical specific energy and the theoretical energy density, but from green (low values) to red (high values) in the case of the theoretical volume change and the energy above hull.

in Figure 3. In the energy related plots the rows for Mg, Ca and Al nicely mirror the advantage of multivalent batteries i.e. high energy density with respect to both, weight and volume. Zn is an exception as it has the least negative standard electrode potential of the analyzed shuttle ions. In order to filter potential high-performance materials we compared the obtained values to state-of-the-art electrode materials investigated on an equal level of theory. Commonly used cathode materials as $LiCoO_2$ (LCO), $LiMn_2O_4$ (LMO), and $LiFePO_4$ (LFP) have for instance been investigated within the PBE+U framework by Chevrier et al.[65] and the derived properties shown in Table 1 serve as reference for the screening in the present work. Although on the material's level, LCO outperforms LMO and LFP by far, the latter

9

two materials suffice the performance criteria of EV batteries[9] which means they can be considered high-energy cathode materials. Thus, we set our screening criteria accordingly. In absolute numbers: We demand a high-performance cathode to possess $\rho_{grav} > 500$ Wh/kg and $\rho_{vol} > 2000$ Wh/dm^3.

The volume change of the electrode upon intercalation is another relevant quantity, as too high values may lead to stress and strain and eventually to pulverization of the material. Visual inspection of Figure 3 shows that in contrary to the energy related properties, which are strongly dependent on the A-site cation, the volume change rather seems to be related to the element on the B-site, although this trend is not as clear. In general, many of the investigated materials, in particular most of the lanthanide containing compounds, show a change in volume of over $20\%_{abs}$ which is the maximum of the color code in Figure 3. Again, we compared these values to the ones derived from Chevrier et al.[65] and set our screening criterion for volume change a bit more loosely to $\frac{\Delta V}{V} < 10\%_{abs}$.

The use of E_{hull} to estimate synthesizability is common practice as has been thoroughly discussed in a recent review.[66] In that regard, $E_{hull} = 0$ indicates that a certain material is positioned on the convex hull and, therefore, claimed to be thermodynamically stable. Nevertheless, due to imperfections of DFT, the negligence of kinetic effects and unknown complications in the synthesis procedure, positive values for E_{hull} may still correspond to synthesizable materials and synthesis of materials with $E_{hull} = 0$ may fail.[66] Here we aim at a criterion to discard all unsynthesizable materials, but the choice of the appropriate threshold value for E_{hull} is a challenging task. Studies similar to the present one use values in the range of 50-100 meV/atom,[51,67] but also smaller thresholds can be found in literature.[47] On the other hand, the authors of the correction scheme we employed[61] report a root mean square error of 92 meV/atom in the prediction of formations energies for a dataset of 222 compounds, which means that outliers may have errors far beyond 100 meV/atom. Therefore, we decided to set the screening criterion to $E_{hull} < 200$ meV. While this value potentially allows many
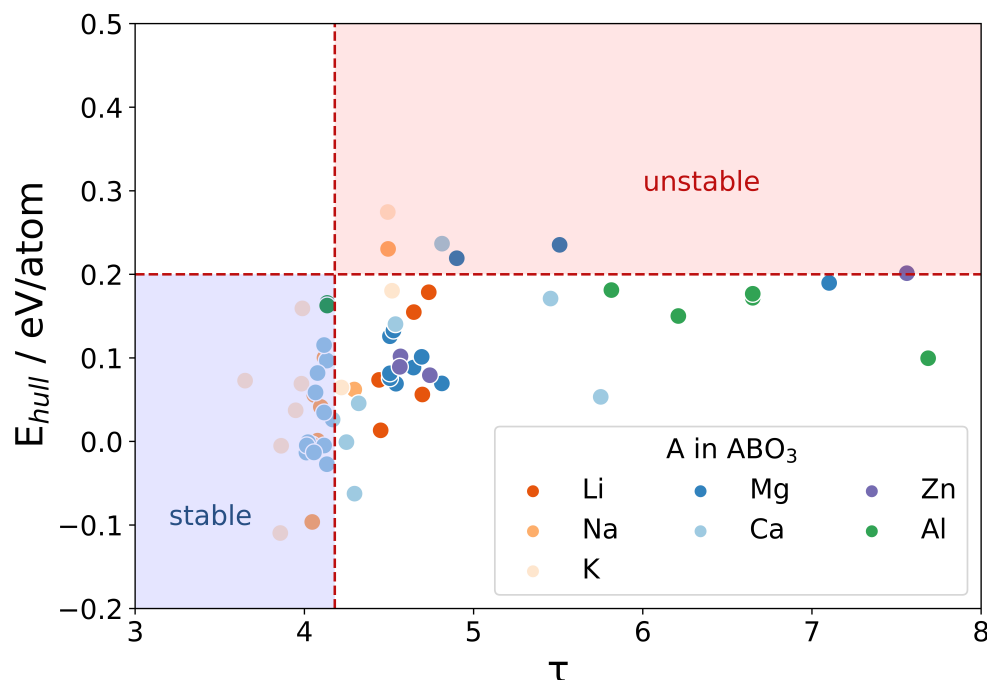
10

Figure 4: Comparison of stability predictions. The stability descriptor τ derived by Bartel et al.[68] is compared with our screening criterion for E_{hull}. The blue left-bottom quadrant contains the compounds which are predicted to be stable by the descriptor method ($\tau <$ 4.18). It is clear that a screening criterion for E_{hull} lower than 200 meV/atom would result in discarding materials which are predicted to be stable by the descriptor method.

unstable materials to pass the stability screening, it insures that the likelyhood of discarding a stable material with potentially promising battery properties is very small.

This approach is further justified by the comparison of our stability predictions to a recent study on the prediction of stable perovskites by a machine learning approach.[68] In this study, the authors designed the stability descriptor τ based on oxidation states and ionic radii, where $\tau < 4.18$ indicates perovskite structure with an accuracy of 92% for oxides. We have evaluated τ for the perovskites of our own dataset where values for the ionic radii were available in the extended list of Ouyang.[69] Figure 4 shows that the descriptor based method predicts stable perovskites up to roughly $E_{hull} = 200$ meV/atom implying that lower threshold values for the screening would possibly lead to the rejection of stable compounds. As a result of the high threshold value, only few compounds ABO_3 are filtered out due to the stability criterion (cf Figure 3). On the contrary, the deintercalated cathode host BO_3 is
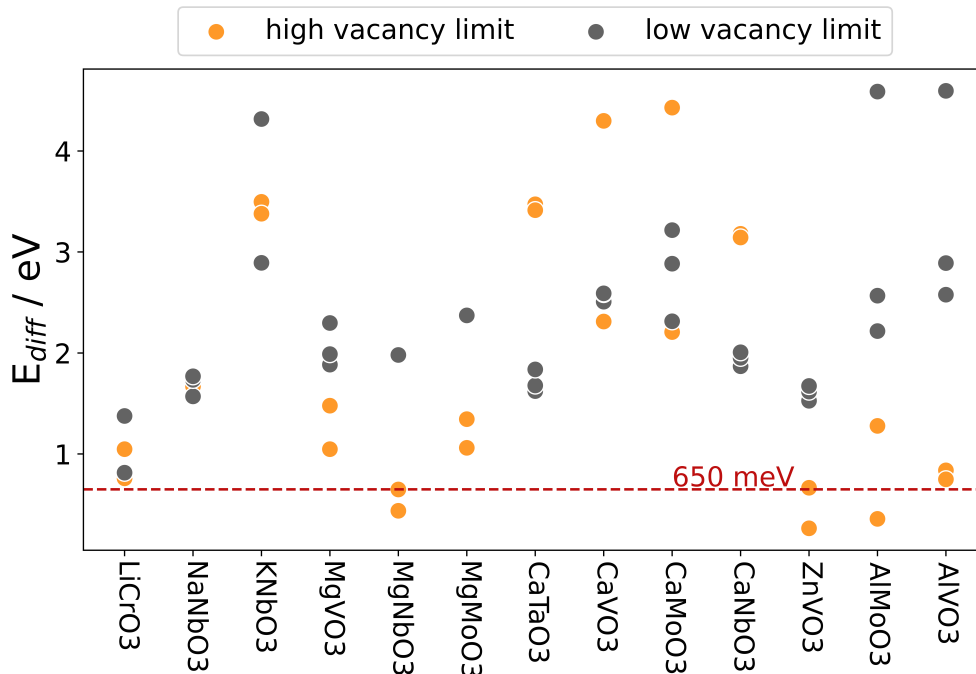
Figure 5: Diffusion barriers for the 13 compounds that have passed the previous screening procedure. All symmetrically non-equivalent diffusion paths are shown in the high vacancy limit and the low vacancy limit. The threshold of 650 meV is depicted as the criterion for sufficient ionic mobility. None of the compounds show barriers below the threshold in the low vacancy limit and $MgNbO_3$, $ZnVO_3$, and $AlMoO_3$ show sufficiently low values in the high vacancy limit.

predicted to be unstable for many B-cations (Al, Si, Sc, Ti, Mn, Co, Ga, Zr, Sn, Sb, Hf, Bi, Ho, Er, Tm, Lu) rendering all corresponding materials as unsuitable for high-energy battery electrodes.

Among the 280 compounds there are 30 which passed the presented screening process. Further 17 were discarded since either for ABO_3 or BO_3 the perovskite structure collapsed during the DFT geometry optimization leaving only 13 compounds for which we determined the energetic barrier for the solid state diffusion of the A-cation. Commonly, 650 meV are assumed as maximum diffusion barrier still allowing sufficient charge/discharge rates in nanostructured materials.[27,70] As shown in Figure 5, none of the perovskite structures in the low vacancy limit and hardly any in the high vacancy limit fulfill this criterion, in contrast to e.g. spinel materials.[71,72] This observation is in line with a previous study on oxide

perovskites. [39,73] Notwithstanding, the screening reveals MgNbO$_3$, ZnVO$_3$, and AlMoO$_3$ as interesting materials exhibiting sufficient mobility in the deintercalated state.

Additionally, it is interesting that the value of E_{diff} strongly differs depending on the exact path taken in the structure. In the case of AlMoO$_3$ for instance, the barrier varies by more than 2 eV within the three paths in the low vacancy limit and by more than 1 eV within the high vacancy limit. A comprehensive study taking all possible diffusion paths into account is thus necessary in the search for a channel for ionic diffusion. A further observation is the discrepancy of the barriers in the low vacancy limit and the high vacancy limit in many cases which amounts to roughly 2eV as in the example of CaTaO$_3$. Since any volume effect on E_{diff} can be excluded due to the imposition of the strongly limiting screening criterion, the discussed discrepancy indicates that the interaction of the shuttle ions on the A-site within the BO$_3$ host structure may significantly affect their ionic mobility.

An overview of the properties of the candidate materials is given in Table 2. While MgNbO$_3$ attains the lowest energy in the rhombohedral symmetry (R$\bar{3}$c), ZnVO$_3$ and AlMoO$_3$ are energetically more favourable in the orthorhomic structure (Pnma). For the materials in the high state of charge the tetragonal structure (P4mm) is attained in all three cases. The specific energy of all three materials is roughly in the range of LMO and LFP or slighty above (compare to Table 1). At the same time, with respect to the energy density, the candidate materials outperform LMO and LFP by far. For instance, the energy density of MgNbO$_3$ is 50 % higher than that of LFP. The energetic performance of LCO, on the

Table 2: Summary of properties. The numerical values of the derived properties for MgNbO$_3$, ZnVO$_3$, and AlMoO$_3$ are shown. In case a compound had several inequivalent diffusion paths only the the value for the lowest barrier is given.

Property	MgNbO$_3$ / NbO$_3$	ZnVO$_3$ / VO$_3$	AlMoO$_3$ / MoO$_3$
spacegroup	R$\bar{3}$c / P4mm	Pnma / P4mm	Pnma / P4mm
ρ_{grav} [Wh/kg]	653	549	709
ρ_{vol} [Wh/dm^3]	3107	2965	3259
min E_{diff} [meV]	1.980 / 438	1527 / 264	2217 / 357
E_{hull} [eV/atom]	104 / 35	79 / 188	129 / -61
$\frac{\Delta V}{V}$ [%$_{abs}$]	6.91	4.75	5.69

13
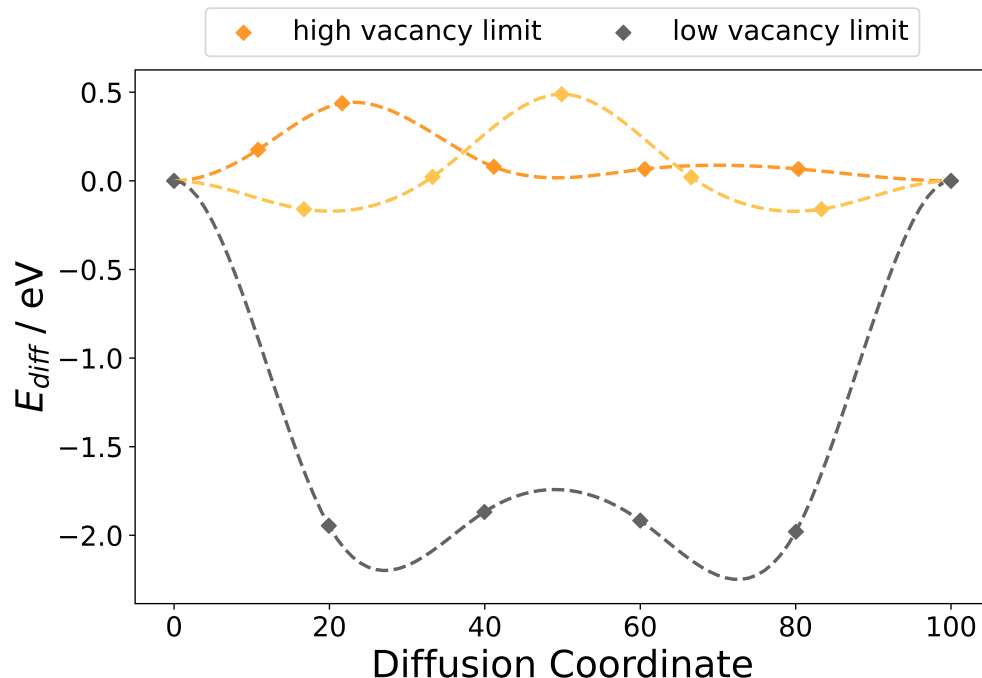
Figure 6: Diffusion barriers of $MgNbO_3$. In the high vacancy limit $MgNbO_3$ exhibits low diffusion barriers. In the low vacancy limit the diffusion path goes downhill indicating that the initial and the final structure are energetically unfavourable for the given stoichiometry. A more detailed discussion can be found in the text.

other hand, could not even be approached. The values for the volume change are reasonably low for all three materials which was ensured by the screening criterion. The values for E_{hull} indicate that NbO_3 and MoO_3 are probably stable materials whereas VO_3 is right under the threshold criterion and therefore not very likely to be stable. The corresponding intercalated compounds $MgNbO_3$, $ZnVO_3$ and, $AlMoO_3$ are located in the intermediate range, i.e. they are potentially, but not very likely, stable.

As discussed above, the diffusion barriers for $MgNbO_3$, $ZnVO_3$, and $AlMoO_3$ in the low vacancy limit are very high, whereas they show promising values in the deintercalated state. A closer look on the diffusion path for $MgNbO_3$ in Figure 6 reveals another interesting fact: The diffusion path in the intercalated material goes downhill. This indicates indeed that the initial and final configurations are not the energetically most favourable ones for the given stoichiometry, but the intermediate images seem to be more stable. We performed DFT

14

geometry optimizations of the distinct images to confirm the outcome of the NEB calculations. The final structures of every image are visualized in the Supporting Information. They reveal that the perovskite-typical corner-sharing oxygen octahedra is retained in every image and the structure does not collapse. Hence, the intermediate images attaining lower energy are still perovskites. This may indicate that the true barrier for solid state diffusion in the low vacancy limit is lower than the value given in Table 2. The barriers for $ZnVO_3$ and $AlMoO_3$ are very high, so electrochemical activity in these compounds is rather unlikely. The diffusion paths for all compounds in Figure 5 are provided in the Supporting Information. Note that also $LiCrO_3$, $MgMoO_3$, and $AlVO_3$ show downhill diffusion paths.

Conclusion

In the present work 280 different oxide perovskites have been investigated as potential high-energy insertion-type cathode materials for batteries. Based on DFT calculations, the specific energy, the energy density, the volume change, and the energy above hull were derived for all compounds. Appropriate screening criteria on these properties were applied to filter out all non-suitable materials. Additionally, it was ensured that the perovskite structure was retained during the DFT geometry optimization. For the 13 materials that passed the screening process the diffusion barriers for the migration of the shuttle ions were derived. Again, a screening criterion ensuring sufficient ionic mobility was employed. None of the investigated compounds exhibited low diffusion barriers in the low vacancy limit and the compounds $MgNbO_3$, $ZnVO_3$, and $AlMoO_3$ only did in the high vacancy limit. After all, we were able to narrow down the initial 280 compounds to the three compounds $MgNbO_3$, $ZnVO_3$, and $AlMoO_3$ which we suggest for further investigation. Of these materials $MgNbO_3$ seems to be particularly promising, as there is reason to believe that the real diffusion barrier for $MgNbO_3$ in the low vacancy limit is considerably lower than suggested by our calculations.

To the best of our knowledge $MgNbO_3$ has never been synthesised, but similar niobate perovskites have been discussed in literature. For instance, ceramic materials within the solid solution $K_xNa_{1-x}NbO_3$ (0<x<1) have been studied due to their promising piezoelectric properties[74,75] and $LiNbO_3$ is known for its ferroelectricity and its optical properties.[76] Even more interesting, high ionic Li mobility was achieved in the defective perovskite material $Li_xLa_{(1-x)/3}NbO_3$,[77–79] but the research has not been extended to other shuttle ions.

In the present study the verifiably existing niobate compounds $LiNbO_3$, $NaNbO_3$, and $KNbO_3$ have been discarded due to high volume change in the case of Li and high diffusion barriers in the case of Na and K. However, our calculations suggest that the Mg intercalated NbO_6 framework could be an interesting research direction in the development of high-energy cathode materials for Mg based batteries.

Acknowledgements

References

(1) McCollum, D.; Krey, V.; Kolp, P.; Nagai, Y.; Riahi, K. Transport electrification: A key element for energy system transformation and climate stabilization. *Clim. Change* **2014**, *123*, 651–664.

16

(2) Zhang, R.; Fujimori, S. The role of transport electrification in global climate change mitigation scenarios. *Environ. Res. Lett.* **2020**, *15*, 034019.

(3) Yuan, M.; Thellufsen, J. Z.; Lund, H.; Liang, Y. The electrification of transportation in energy transition. *Energy* **2021**, *236*, 121564.

(4) Ramachandran, S.; Stimming, U. Well to wheel analysis of low carbon alternatives for road traffic. *Energy Environ. Sci.* **2015**, *8*, 3313–3324.

(5) Ueckerdt, F.; Bauer, C.; Dirnaichner, A.; Everall, J.; Sacchi, R.; Luderer, G. Potential and risks of hydrogen-based e-fuels in climate change mitigation. *Nat. Clim. Change* **2021**, *11*, 384–393.

(6) Ziegler, M. S.; Trancik, J. E. Re-examining rates of lithium-ion battery technology improvement and cost decline. *Energy Environ. Sci.* **2021**, *14*, 1635–1651.

(7) Edelenbosch, O. Y.; Hof, A. F.; Nykvist, B.; Girod, B.; van Vuuren, D. P. Transport electrification: the effect of recent battery cost reduction on future emission scenarios. *Clim. Change* **2018**, *151*, 95–108.

(8) Martins, L. S.; Guimarães, L. F.; Botelho Junior, A. B.; Tenório, J. A. S.; Espinosa, D. C. R. Electric car battery: An overview on global demand, recycling and future approaches towards sustainability. *J. Environ. Manage.* **2021**, *295*, 113091.

(9) Fichtner, M. Recent Research and Progress in Batteries for Electric Vehicles. *Batteries Supercaps* **2022**, *5*, e202100224.

(10) Holland, S. P.; Mansur, E. T.; Muller, N. Z.; Yates, A. J. The environmental benefits of transportation electrification: Urban buses. *Energy Policy* **2021**, *148*, 111921.

(11) Kersey, J.; Popovich, N. D.; Phadke, A. A. Rapid battery cost declines accelerate the prospects of all-electric interregional container shipping. *Nat. Energy* **2022**, *7*, 664–674.

17

(12) Ziemann, S.; Müller, D. B.; Schebek, L.; Weil, M. Modeling the potential impact of lithium recycling from EV batteries on lithium demand: A dynamic MFA approach. *Resour., Conserv. Recycl.* **2018**, *133*, 76–85.

(13) Sovacool, B. K.; Ali, S. H.; Bazilian, M.; Radley, B.; Nemery, B.; Okatz, J.; Mulvaney, D. Sustainable minerals and metals for a low-carbon future. *Science* **2020**, *367*, 30–33.

(14) Pulido-Sánchez, D.; Capellán-Pérez, I.; de Castro, C.; Frechoso, F. Material and energy requirements of transport electrification. *Energy Environ. Sci.* **2022**, *15*, 4872–4910.

(15) Peters, J. F.; Baumann, M.; Zimmermann, B.; Braun, J.; Weil, M. The environmental impact of Li-Ion batteries and the role of key parameters – A review. *Renewable Sustainable Energy Rev.* **2017**, *67*, 491–506.

(16) Harper, G.; Sommerville, R.; Kendrick, E.; Driscoll, L.; Slater, P.; Stolkin, R.; Walton, A.; Christensen, P.; Heidrich, O.; Lambert, S.; Abbott, A.; Ryder, K.; Gaines, L.; Anderson, P. Recycling lithium-ion batteries from electric vehicles. *Nature* **2019**, *575*, 75–86.

(17) Larcher, D.; Tarascon, J.-M. Towards greener and more sustainable batteries for electrical energy storage. *Nat. Chem.* **2015**, *7*, 19–29.

(18) Bauer, C. et al. Charging sustainable batteries. *Nat. Sustain.* **2022**, *5*, 176–178.

(19) Titirici, M. et al. The sustainable materials roadmap. *J. Phys Mater.* **2022**, *5*, 032001.

(20) Rothgang, S.; Rogge, M.; Becker, J.; Sauer, D. U. Battery Design for Successful Electrification in Public Transport. *Energies* **2015**, *8*, 6715–6737.

(21) Xu, C.; Dai, Q.; Gaines, L.; Hu, M.; Tukker, A.; Steubing, B. Future material demand for automotive lithium-based batteries. *Commun. Mater.* **2020**, *1*, 99.

18

(22) Qiu, T.; Yu, Z.; Xie, W.; He, Y.; Wang, H.; Zhang, T. Preparation of Onion-like Synthetic Graphite with a Hierarchical Pore Structure from Anthracite and Its Electrochemical Properties as the Anode Material of Lithium-Ion Batteries. *Energy Fuels* **2022**, *36*, 8256–8266.

(23) Chayambuka, K.; Mulder, G.; Danilov, D. L.; Notten, P. H. L. From Li-Ion Batteries toward Na-Ion Chemistries: Challenges and Opportunities. *Adv. Energy Mater.* **2020**, *10*, 2001310.

(24) Euchner, H.; Vinayan, B. P.; Reddy, M. A.; Fichtner, M.; Groß, A. Alkali metal insertion into hard carbon – the full picture. *J. Mater. Chem. A* **2020**, *8*, 14205–14213.

(25) Ma, Y.; Ma, Y.; Euchner, H.; Liu, X.; Zhang, H.; Qin, B.; Geiger, D.; Biskupek, J.; Carlsson, A.; Kaiser, U.; Groß, A.; Indris, S.; Passerini, S.; Bresser, D. An Alternative Charge-Storage Mechanism for High-Performance Sodium-Ion and Potassium-Ion Anodes. *ACS Energy Lett.* **2021**, *6*, 915–924.

(26) Post Lithium Storage (POLIS) - Cluster of Excellence. 2017; https://www.postlithiumstorage.org.

(27) Canepa, P.; Sai Gautam, G.; Hannah, D. C.; Malik, R.; Liu, M.; Gallagher, K. G.; Persson, K. A.; Ceder, G. Odyssey of Multivalent Cathode Materials: Open Questions and Future Challenges. *Chem. Rev.* **2017**, *117*, 4287–4341.

(28) Tian, Y.; Zeng, G.; Rutt, A.; Shi, T.; Kim, H.; Wang, J.; Koettgen, J.; Sun, Y.; Ouyang, B.; Chen, T.; Lun, Z.; Rong, Z.; Persson, K.; Ceder, G. Promises and Challenges of Next-Generation "Beyond Li-ion" Batteries for Electric Vehicles and Grid Decarbonization. *Chem. Rev.* **2021**, *121*, 1623–1669.

(29) Schroeder, M. A.; Ma, L.; Pastel, G.; Xu, K. The mystery and promise of multivalent metal-ion batteries. *Curr. Opin. Electrochem.* **2021**, *29*, 100819.

(30) Maroni, F.; Dongmo, S.; Gauckler, C.; Marinaro, M.; Wohlfahrt-Mehrens, M. Through the Maze of Multivalent-Ion Batteries: A Critical Review on the Status of the Research on Cathode Materials for Mg^{2+} and Ca^{2+} Ions Insertion. *Batteries Supercaps* **2021**, *4*, 1221–1251.

(31) Alfaruqi, M. H.; Lee, S.; Kang, H.; Sambandam, B.; Mathew, V.; Hwang, J.-Y.; Kim, J. Recent Achievements in Experimental and Computational Studies of Positive Electrode Materials for Nonaqueous Ca- and Al-Ion Batteries. *J. Phys. Chem. C* **2022**, *126*, 9209–9227.

(32) Katz, E. A. Perovskite: Name Puzzle and German-Russian Odyssey of Discovery. *Helv. Chim. Acta* **2020**, *103*, e2000061.

(33) Bhalla, A. S.; Guo, R.; Roy, R. The perovskite structure—a review of its role in ceramic science and technology. *Mater. Res. Innovations* **2000**, *4*, 3–26.

(34) Hwang, J.; R. Rao, R.; Giordano, L.; Katayama, Y.; Yu, Y.; Shao-Horn, Y. Perovskites in catalysis and electrocatalysis. *Science* **2017**, *358*, 751–756.

(35) Sun, C.; Alonso, J. A.; Bian, J. Recent Advances in Perovskite-Type Oxides for Energy Conversion and Storage Applications. *Adv. Energy Mater.* **2021**, *11*, 2000459.

(36) Cao, Y.; Liang, J.; Li, X.; Yue, L.; Liu, Q.; Lu, S.; Asiri, A. M.; Hu, J.; Luo, Y.; Sun, X. Recent advances in perovskite oxides as electrode materials for supercapacitors. *Chem. Commun.* **2021**, *57*, 2343–2355.

(37) Sun, Y.; Guan, P.; Liu, Y.; Xu, H.; Li, S.; Chu, D. Recent Progress in Lithium Lanthanum Titanate Electrolyte towards All Solid-State Lithium Ion Secondary Battery. *Crit. Rev. Solid State Mater. Sci.* **2019**, *44*, 265–282.

(38) Pérez-Vicente, C.; Medina, A.; Alcántara, R. A Comparative View of Alkaline and Alkaline-Earth Element Intercalation into Perovskite-Type $A_x La_y TiO_3$ (A = Li, Na,

(39) Arroyo-de Dompablo, M. E.; Krich, C.; Nava-Avendaño, J.; Palacín, M. R.; Bardé, F. In quest of cathode materials for Ca ion batteries: the $CaMO_3$ perovskites (M = Mo, Cr, Mn, Fe, Co, and Ni). *Phys. Chem. Chem. Phys.* **2016**, *18*, 19966–19972.

(40) Pathreeker, S.; Reed, S.; Chando, P.; Hosein, I. D. A study of calcium ion intercalation in perovskite calcium manganese oxide. *J. Electroanal. Chem.* **2020**, *874*, 114453.

(41) Euchner, H.; Groß, A. Atomistic modeling of Li- and post-Li-ion batteries. *Phys. Rev. Mater.* **2022**, *6*, 040302.

(42) Glazer, A. M. A brief history of tilts. *Phase Transitions* **2011**, *84*, 405–420.

(43) Howard, C. J.; Stokes, H. T. Group-Theoretical Analysis of Octahedral Tilting in Perovskites. *Acta Cryst. B* **1998**, *54*, 782–789.

(44) Stokes, H. T.; Kisi, E. H.; Hatch, D. M.; Howard, C. J. Group-theoretical analysis of octahedral tilting in ferroelectric perovskites. *Acta Cryst. B* **2002**, *58*, 934–938.

(45) Xie, N.; Zhang, J.; Raza, S.; Zhang, N.; Chen, X.; Wang, D. Generation of low-symmetry perovskite structures for ab initio computation. *J. Phys. Condens. Matter* **2020**, *32*, 315901.

(46) Emery, A. A.; Wolverton, C. High-throughput DFT calculations of formation energy, stability and oxygen vacancy formation energy of ABO_3 perovskites. *Sci. Data* **2017**, *4*, 170153.

(47) Schmidt, J.; Shi, J.; Borlido, P.; Chen, L.; Botti, S.; Marques, M. A. L. Predicting the Thermodynamic Stability of Solids Combining Density Functional Theory and Machine Learning. *Chem. Mater.* **2017**, *29*, 5090–5103.

21

(48) Perdew, J. P.; Burke, K.; Ernzerhof, M. Generalized Gradient Approximation Made Simple. *Phys. Rev. Lett.* **1996**, *77*, 3865–3868.

(49) Zhou, F.; Cococcioni, M.; Marianetti, C. A.; Morgan, D.; Ceder, G. First-principles prediction of redox potentials in transition-metal compounds with LDA+U. *Phys. Rev. B* **2004**, *70*, 235121.

(50) Mahlberg, D.; Sakong, S.; Forster-Tonigold, K.; Groß, A. Improved DFT Adsorption Energies with Semiempirical Dispersion Corrections. *J. Chem. Theory Comput.* **2019**, *15*, 3250–3259.

(51) Sotoudeh, M.; Dillenz, M.; Döhn, J.; Hansen, J.; Dsoke, S.; Groß, A. Oxide Spinels with Superior Mg Conductivity. *Chem. Mater.* **2023**, *35*, 4786–4797.

(52) Dudarev, S. L.; Botton, G. A.; Savrasov, S. Y.; Humphreys, C. J.; Sutton, A. P. Electron-energy-loss spectra and the structural stability of nickel oxide: An LSDA+U study. *Phys. Rev. B* **1998**, *57*, 1505–1509.

(53) Jain, A.; Ong, S. P.; Hautier, G.; Chen, W.; Richards, W. D.; Dacek, S.; Cholia, S.; Gunter, D.; Skinner, D.; Ceder, G.; Persson, K. A. Commentary: The Materials Project: A materials genome approach to accelerating materials innovation. *APL Mater.* **2013**, *1*, 011002.

(54) Blöchl, P. E. Projector augmented-wave method. *Phys. Rev. B* **1994**, *50*, 17953–17979.

(55) Kresse, G.; Hafner, J. Ab initio molecular dynamics for liquid metals. *Phys. Rev. B* **1993**, *47*, 558–561.

(56) Kresse, G.; Furthmüller, J. Efficient iterative schemes for ab initio total-energy calculations using a plane-wave basis set. *Phys. Rev. B* **1996**, *54*, 11169–11186.

(57) Kresse, G.; Joubert, D. From ultrasoft pseudopotentials to the projector augmented-wave method. *Phys. Rev. B* **1999**, *59*, 1758–1775.

(58) Chang, J.; Chen, Q.; Ma, L.; Li, C.; Peng, Y.; Wu, W.; Wang, H. On the electronic structure and magnetism of $CaCrO_3$: A hybrid-exchange density-functional-theory study. *Mater. Today Commun.* **2021**, *27*, 102179.

(59) Jain, A.; Hautier, G.; Moore, C. J.; Ong, S. P.; Fischer, C. C.; Mueller, T.; Persson, K. A.; Ceder, G. A high-throughput infrastructure for density functional theory calculations. *Comput. Mater. Sci.* **2011**, *50*, 2295–2310.

(60) Horton, M. K.; Montoya, J. H.; Liu, M.; Persson, K. A. High-throughput prediction of the ground-state collinear magnetic order of inorganic materials using Density Functional Theory. *npj Comput. Mater.* **2019**, *5*, 64.

(61) Wang, A.; Kingsbury, R.; McDermott, M.; Horton, M.; Jain, A.; Ong, S. P.; Dwaraknath, S.; Persson, K. A. A framework for quantifying uncertainty in DFT energy corrections. *Sci. Rep.* **2021**, *11*, 15496.

(62) Henkelman, G.; Jónsson, H. A dimer method for finding saddle points on high dimensional potential surfaces using only first derivatives. *J. Chem. Phys.* **1999**, *111*, 7010.

(63) Sheppard, D.; Terrell, R.; Henkelman, G. Optimization methods for finding minimum energy paths. *J. Chem. Phys.* **2008**, *128*, 134106.

(64) Henkelman, G.; Uberuaga, B. P.; Jónsson, H. A climbing image nudged elastic band method for finding saddle points and minimum energy paths. *J. Chem. Phys.* **2000**, *113*, 9901–9904.

(65) Chevrier, V. L.; Ong, S. P.; Armiento, R.; Chan, M. K. Y.; Ceder, G. Hybrid density functional calculations of redox potentials and formation energies of transition metal compounds. *Phys. Rev. B* **2010**, *82*, 075122.

(66) Bartel, C. J. Review of computational approaches to predict the thermodynamic stability of inorganic solids. *J. Mater. Sci.* **2022**, *57*, 10475–10498.

(67) Rutt, A.; Shen, J.-X.; Horton, M.; Kim, J.; Lin, J.; Persson, K. A. Expanding the Material Search Space for Multivalent Cathodes. *ACS Appl. Mater. Interfaces* **2022**, *14*, 44367–44376.

(68) Bartel, C. J.; Sutton, C.; Goldsmith, B. R.; Ouyang, R.; Musgrave, C. B.; Ghiringhelli, L. M.; Scheffler, M. New tolerance factor to predict the stability of perovskite oxides and halides. *Sci. Adv.* **2019**, *5*, eaav0693.

(69) Ouyang, R. Exploiting Ionic Radii for Rational Design of Halide Perovskites. *Chem. Mater.* **2020**, *32*, 595–604.

(70) Rong, Z.; Malik, R.; Canepa, P.; Sai Gautam, G.; Liu, M.; Jain, A.; Persson, K.; Ceder, G. Materials Design Rules for Multivalent Ion Mobility in Intercalation Structures. *Chem. Mater.* **2015**, *27*, 6016–6021.

(71) Canepa, P.; Bo, S.-H.; Gautam, G. S.; Key, B.; Richards, W. D.; Shi, T.; Tian, Y.; Wang, Y.; Li, J.; Ceder, G. High magnesium mobility in ternary spinel chalcogenides. *Nat. Comm.* **2017**, *8*, 1–8.

(72) Dillenz, M.; Sotoudeh, M.; Glaser, C.; Janek, J.; Groß, A.; Euchner, H. Unravelling Charge Carrier Mobility in d0-Metal-based Spinels. *Batteries & Supercaps* **2022**, *5*, e202200164.

(73) Sotoudeh, M.; Groß, A. Descriptor and Scaling Relations for Ion Mobility in Crystalline Solids. *JACS Au* **2022**, *2*, 463–471.

(74) Zhang, N.; Zheng, T.; Wu, J. Lead-Free $(K,Na)NbO_3$-Based Materials: Preparation Techniques and Piezoelectricity. *ACS Omega* **2020**, *5*, 3099–3107.

(75) Bidaraguppe Ramesh, N.; Schmidt, F.; Schindlmayr, A. Lattice parameters and electronic bandgap of orthorhombic potassium sodium niobate $K_{0.5}Na_{0.5}NbO_3$ from density-functional theory. *Eur. Phys. J. B* **2021**, *94*, 169.

(76) Guithi, K.; Sekrafi, H. E.; Kharrat, A. B. J.; Khirouni, K.; Boujelben, W. Synthesis, structural and optical characterization of $LiNbO_3$ material for optical applications. *J. Opt.* **2023**,

(77) Belous, A.; Pashkova, E.; Gavrilenko, O.; V'yunov, O.; Kovalenko, L. Solid electrolytes based on lithium-containing lanthanum metaniobates. *J. Eur. Ceram. Soc.* **2004**, *24*, 1301–1304.

(78) Hong, J.; Kobayashi, S.; Kuwabara, A.; Ikuhara, Y. H.; Fujiwara, Y.; Ikuhara, Y. Defect Engineering and Anisotropic Modulation of Ionic Transport in Perovskite Solid Electrolyte $Li_xLa_{(1-x)/3}NbO_3$. *Molecules* **2021**, *26*.

(79) Yang, Z.; Suzuki, S.; Tanibata, N.; Takeda, H.; Nakayama, M.; Karasuyama, M.; Takeuchi, I. Efficient Experimental Search for Discovering a Fast Li-Ion Conductor from a Perovskite-Type $Li_xLa_{(1-x)/3}NbO_3$ (LLNO) Solid-State Electrolyte Using Bayesian Optimization. *J. Phys. Chem. C* **2021**, *125*, 152–160.

(80) Momma, K.; Izumi, F. VESTA3 for three-dimensional visualization of crystal, volumetric and morphology data. *J. Appl. Crystallogr.* **2011**, *44*, 1272–1276.